



# First-principles soft-mode lattice dynamics of $\text{PbZr}_{0.5}\text{Ti}_{0.5}\text{O}_3$ and shortcomings of the virtual crystal approximation

Jack S. Baker  and David R. Bowler 

*London Centre for Nanotechnology, UCL, 17–19 Gordon Street, London WC1H 0AH, United Kingdom  
and Department of Physics and Astronomy, UCL, Gower Street, London WC1E 6BT, United Kingdom*



(Received 4 October 2019; revised manuscript received 27 November 2019; published 20 December 2019)

A comparative study of  $\text{PbTiO}_3$ ,  $\text{PbZrO}_3$ , and the solid solution  $\text{PbZr}_{0.5}\text{Ti}_{0.5}\text{O}_3$  is performed on the soft-mode lattice dynamics within the first Brillouin zone. We consider the six unique B-site orderings for  $\text{PbZr}_{0.5}\text{Ti}_{0.5}\text{O}_3$  representable within the  $2 \times 2 \times 2$  primitive perovskite supercell as well as the virtual crystal approximation (VCA) to extract the phonon dispersion relations of a high-symmetry cubic-constrained form using density functional perturbation theory. We find that the most unstable modes in the rock-salt ordered structure and the VCA, like pure  $\text{PbZrO}_3$ , are antiferrodistortive (AFD) while lower symmetry arrangements are dominated by  $\Gamma$ -point ferroelectric (FE) instabilities like pure  $\text{PbTiO}_3$ . Despite similarities in the phonon dispersion relations between the rock-salt ordered supercell and the VCA, the character of modes at high symmetry points are found to be different. In particular, the  $a^0a^0c^-$  and  $a^0a^0c^+$  AFD instabilities of the rock-salt ordering are replaced with  $a^-b^-c^-$  and  $a^+b^+c^+$  instabilities within the VCA. Such a rotation pattern is not seen in any of the supercell-based calculations, thus serving as a quantitative example of the inability of the method to accurately represent local structural distortions. Single modes are found exhibiting dual order parameters. At the zone center, some arrangements show mixed FE and antipolar soft modes (due to Pb motion transverse to the polar axis), and at long wavelengths all arrangements have soft modes of a mixed antipolar and AFD character. These are described with direct analysis of the eigendisplacements.

DOI: [10.1103/PhysRevB.100.224305](https://doi.org/10.1103/PhysRevB.100.224305)

## I. INTRODUCTION

The  $\text{PbZr}_x\text{Ti}_{1-x}\text{O}_3$  (PZT) solid solution is the most abundantly used piezoelectric material. This is due to its giant electromechanical response and well-developed, low-cost synthesis [1,2]. Together, this has ensured the technological relevance of the material, which is well adapted for exploitation in ultrasonic transducers [3,4], ceramic capacitors, and actuators [5]. More exotically, PZT has been proposed for use in potential piezoelectricity induced room-temperature superconductors where a supercurrent is induced along a metal/piezoelectric interface [6,7]. For these applications, it is most common to consider PZT at around  $x \approx 0.52$  [8,9] in the region near the morphotropic phase boundary (MPB). This is a compositional boundary at the peak of the electromechanical response. This boundary exhibits complex lattice dynamics where a flat energy surface for polarization rotation exists between the FE tetragonal ( $\mathbf{P} \parallel [001]$ ) and rhombohedral ( $\mathbf{P} \parallel [111]$ ) phases via intermediate monoclinic phases [8,10,11].

It is useful to regard PZT as a randomly ordered isovalent B-site substituted compound in a matrix of either of the two phase diagram end members  $\text{PbTiO}_3$  (PTO) or  $\text{PbZrO}_3$  (PZO). The former is a prototypical FE with  $P4mm$  symmetry [12] while the latter, though still topical [13–17], is considered an antiferroelectric (AFE) with  $Pbam$  symmetry. These observations are supported using the soft-mode theory of lattice dynamics by considering the symmetry (and energy) lowering distortions of a high-symmetry cubic phase as indicated by imaginary frequencies at certain wave vectors in the phonon spectrum [18–21]. It is using this method that the modes

responsible for the paraelectric to FE transition in PTO and paraelectric to AFE transition in PZO are identified as  $\Gamma_4^-$  [12,22] and dual  $\Sigma_2 + R_4^+$  (and to a lesser extent,  $S_4$ ,  $R_5^+$ ,  $X_3^-$ , and  $M_5^-$ ) [15,17] respectively. Such a classification is not possible for a truly random alloy. Even for ordered PZT, it proves much more difficult since the character and frequencies of the relevant modes may vary with Ti/Zr concentration as well as with the specific ordering of the B-site substitutions in the crystal lattice, for which in a periodic crystal the number of permutations are infinite.

In order to study PZT near the MPB with first-principles calculations, we consider two paths. Both paths impose fictitious symmetry when compared to the real random compound. The first is to explore the different permutations of Ti/Zr substitutions within a supercell of finite size. True morphotropic PZT requires simulation in a large supercell, so  $x = 0.5$  is often chosen as a surrogate. This is the most common approach taken and has been successful in the calculation of structural [23,24], piezoelectric [25,26], and electronic properties [27]. Using this method, phonon dispersion relations across a small area of the first Brillouin zone have also been calculated for [1:1] PZO/PTO superlattices [28]. For (001) and (110) ordered structures, FE modes were isolated to Ti/Zr layers while the (111) ordered superlattice displays one mode behavior with competing FE and AFD character. This study, however, was limited in scope by only considering modes at the zone center. The second option is to use a mixed potential scheme such as the VCA. This approach, like the supercell method, predicts anomalous dynamical charges and, with reasonable accuracy, the location of the MPB [29–31] but

is unable to accurately represent distortions to local structure. The extent to which this is true, however, is unknown; thus, a quantitative comparison based on the characteristics of the soft-mode distortions would be valuable. This approach, however, does allow access to a wide range of Ti/Zr concentrations at a fraction of the computational cost of a large supercell calculation.

It is the aim of this work to provide a complete comparative study of the phonon dispersion relations in near-morphotropic  $\text{PbZr}_{0.5}\text{Ti}_{0.5}\text{O}_3$  within density functional theory (DFT) using the VCA and supercell method complete with comparison to the end members PTO and PZO. We do so also with special consideration of longer wavelength modes often not considered. We compare the characters of soft modes by considering distortions at high symmetry points via eigendisplacement analysis and the projected phonon density of states (PDOS). Doing so gives access to displacement patterns and to the species-specific character of all modes in the soft space. We select the  $2 \times 2 \times 2$  supercell of the primitive perovskite unit for our simulations to coincide with measured mean cluster size distributions for Ti/Zr ordering in PZT [32]. Such supercells have recently been used as local phases to build a complex multiphase model of the material able to predict the experimental pair distribution function to a high accuracy [33]. Such a supercell dimension is also important for theoretical studies since important competitive modes including Glazer-like [34,35] AFD, FE, and some AFE modes fold to the zone center. However, since our calculations are performed throughout the full first Brillouin zone, we are not limited to the zone center and so we can identify competitive long-wavelength order not usually considered in PZT. We obtain the irreducible representations (irreps) of the soft-mode distortions and identify their incipient order parameters which in the case of longer wavelength modes we find can impose dual order. By doing so, we provide further insight into the complex lattice dynamics occurring near the MPB. Further, it will provide a guide for future investigations detailing the consequences of using the supercell or VCA methods for future studies of PZT and heterostructures for which PZT is an ingredient.

The rest of this work is organized as follows. In Sec. II, we detail the theoretical methods for the calculations, including details for the calculation of the electronic ground state, phonon dispersions, and details for the specific implementation of the VCA. In Sec. III A, we discuss the properties of the fully relaxed parent structures. Then, in Sec. III B, we present the full phonon dispersion relations and PDOS along with a discussion and tabulation of the relevant soft modes and their frequencies. We begin first with a comparison between the end members PTO and PZO. The other dispersions are then paired based on their similarity and discussed together with the exception of  $Pm\bar{3}m$  ordered PZT supercell, which has its own dedicated section. Modes important to the discussion are shown graphically. These results are then discussed more broadly and summarized in Sec. IV.

## II. THEORETICAL METHOD

Calculations are performed using the implementation of DFT as present in the ABINIT code (v8.10.2) [36,37]. We

use scalar-relativistic, norm-conserving pseudopotentials generated by the ONCVSP code (v3.3.0) [38] as made available on the PseudoDojo website [39]. These potentials treat the  $\text{Pb } 5d^{10}6s^26p^6$ ,  $\text{Ti } 3s^23p^64s^23d^{10}$ ,  $\text{Zr } 4s^24p^65s^25d^{10}$ , and  $\text{O } 2s^22p^6$  orbitals as valence. These pseudopotentials include partial core corrections. For the  $2 \times 2 \times 2$  supercells, Brillouin zone integrals are performed with sums over  $\Gamma$ -centered  $4 \times 4 \times 4$  Monkhorst-Pack [40] meshes. A plane-wave cutoff energy of 1088.46 eV (40 Ha) is employed to ensure the accuracy of our calculations. Exchange and correlation effects are represented by the PBESol [41] functional as present in Libxc (v3.0.0) [42]. This functional is known to produce high-accuracy structural properties compared with experimental results [43], justifying its use in a study of structural distortion. This method returns the paraelectric cubic  $Pm\bar{3}m$  lattice constants of PTO and PZO as  $a_{\text{PTO}} = 3.918 \text{ \AA}$  ( $-0.304\%$ ) and  $a_{\text{PZO}} = 4.140 \text{ \AA}$  ( $+0.242\%$ ), where bracketed values are errors compared with experimental results [44,45]. We make particular use of the linear response features in ABINIT for the calculation of phonon dispersions using density functional perturbation theory (DFPT) [46,47]. Dynamical matrices are calculated on the  $\mathbf{q}$ -point mesh of the supercell calculation and dispersion is extracted using a Fourier interpolation scheme

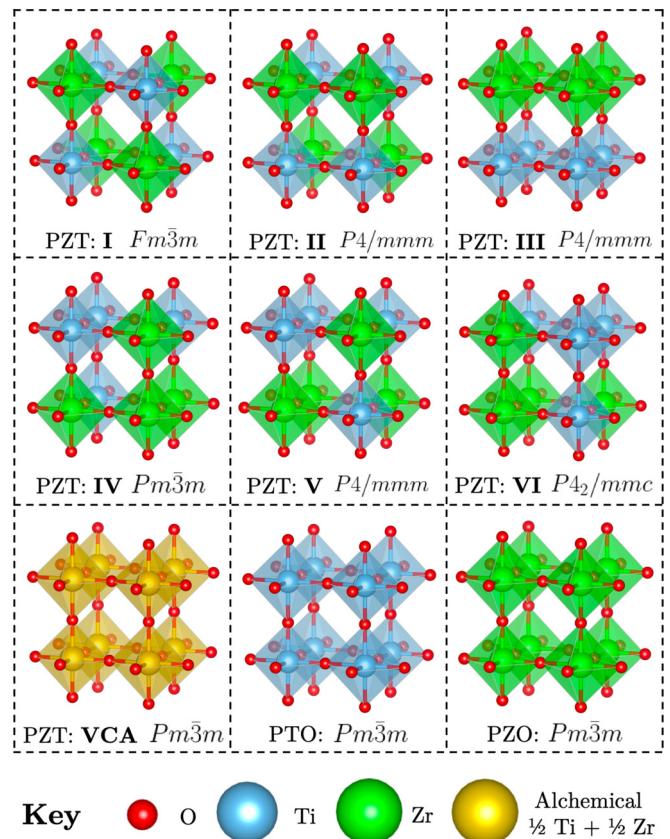


FIG. 1. The structures used for the phonon dispersion calculations of Sec. III B. A-site Pb has been removed for clarity and  $\text{BO}_6$  octahedral complexes have been colored to match the B-site species. Supercell models (rows 1 and 2) are labeled with Roman numerals I–VI while the last row indicates the PZT-VCA supercell as well as the end members PTO and PZO. Each supercell is also assigned a crystalline space group.

between points on the  $\mathbf{q}$ -point mesh [46,47]. Since the perovskite oxides are known to give rise to giant longitudinal optical-transverse optical (LO-TO) splitting [48], we require the nonanalytic correction (NAC) at the  $\Gamma$  point [46] to

TABLE I. The space groups, Wyckoff positions, and *primitive* supercell dimensions of the relaxed, cubic-constrained structures. All structures are representable in the  $2 \times 2 \times 2$  primitive perovskite supercell as illustrated in Fig. 1. Wyckoff positions are stated using the site multiplicity and Wyckoff letter as made standard by the Bilbao Crystallographic Server [59]. Supercell dimensions are given in lengths of the mutually orthogonal axes  $a$ ,  $b$ , and  $c$  with the exception of PZT I, whose axes are at an angle  $\alpha = \beta = \gamma = 60^\circ$  with the full form of the lattice vectors displayed.

PTO/PZO/VCA ( $Pm\bar{3}m O_h^1$ )	
$a = a_{\text{PTO}}/a_{\text{PZO}}/a_{\text{Vg}}$	
Pb 1b	(1/2, 1/2, 1/2)
Ti/Zr/(1/2 Ti + 1/2 Zr) 1a	(0, 0, 0)
O 3d	(1/2, 0, 0)
PZT: I ( $Fm\bar{3}m O_h^5$ )	
$\mathbf{a} = (0, a_{\text{Vg}}, a_{\text{Vg}})$ , $\mathbf{b} = (a_{\text{Vg}}, 0, a_{\text{Vg}})$ , $\mathbf{c} = (a_{\text{Vg}}, a_{\text{Vg}}, 0)$	
Pb 2c	(1/4, 1/4, 1/4)
Zr 1a	(0, 0, 0)
O 6e	( $x, 0, 0$ ), $x = 0.74232$
Ti 1b	(1/2, 1/2, 1/2)
PZT: II ( $P4/mmm D_{4h}^1$ )	
$a = \sqrt{2}a_{\text{Vg}}$ , $b = \sqrt{2}a_{\text{Vg}}$ , $c = a_{\text{Vg}}$	
Pb 2f	(0, 1/2, 0)
Zr 1d	(1/2, 1/2, 1/2)
Ti 1b	(0, 0, 1/2)
O 4k	( $x, x, 1/2$ ), $x = 0.75838$
O 1c	(1/2, 1/2, 0)
O 1a	(0, 0, 0)
PZT: III ( $P4/mmm D_{4h}^1$ )	
$a = b = a_{\text{Vg}}$ , $c = 2a_{\text{Vg}}$	
Pb 2g	(0, 0, $x$ ), $x = 0.26377$
Zr 1c	(1/2, 1/2, 0)
Ti 1d	(1/2, 1/2, 1/2)
O 2f	(0, 1/2, 0)
O 2h	(1/2, 1/2, $x$ ), $x = 0.26279$
O 2e	(1/2, 1/2, 1/2)
PZT: IV ( $Pm\bar{3}m O_h^1$ )	
$a = 2a_{\text{Vg}}$	
Pb 8g	( $x, x, x$ ), $x = 0.74307$
Zr 1a	(0, 0, 0)
Zr 3d	(1/2, 1/2, 0)
Ti 3c	(0, 1/2, 1/2)
Ti 1b	(1/2, 1/2, 1/2)
O 6e	( $x, 0, 0$ ), $x = 0.74807$
O 12h	( $x, 1/2, 0$ ), $x = 0.26024$
O 6f	( $x, 1/2, 1/2$ ), $x = 0.74667$
PZT: V ( $P4/mmm D_{4h}^1$ )	
$a = 2a_{\text{Vg}}$	
Pb 8r	( $x, x, z$ ), $x = 0.75030$ , $z = 0.74302$

TABLE I. (*continued.*)

Zr 1a	(0, 0, 0)
Zr 2f	(0, 1, 2, 0)
Zr 1d	(1/2, 1/2, 1/2)
Ti 1b	(0, 0, 1/2)
Ti 2e	(0, 1/2, 1/2)
Ti 1c	(1/2, 1/2, 0)
O 4l	( $x, 0, 0$ ), $x = 0.74975$
O 2g	(0, 0, $z$ ), $z = 0.73908$
O 4m	( $x, 0, 1/2$ ), $x = 0.75053$
O 4n	( $x, 1/2, 0$ ), $x = 0.74198$
O 4i	(0, 1/2, $z$ ), $z = 0.73972$
O 4o	( $x, 1/2, 1/2$ ), $x = 0.75804$
O 2h	(1/2, 1/2, $z$ ), $z = 0.75582$
PZT: VI ( $P4_2/mmc D_{4h}^9$ )	
$a = 2a_{\text{Vg}}$	
Pb 8n	( $x, x, 1/4$ ), $x = 0.25710$
Zr 2a	(0, 0, 0)
Zr 2c	(0, 1/2, 0)
Ti 2d	(0, 1/2, 1/2)
Ti 2b	(1/2, 1/2, 0)
O 2e	(0, 0, 1/4)
O 2l	( $x, 0, 1/2$ ), $x = 0.25134$
O 4j	( $x, 0, 0$ ), $x = 0.26117$
O 4i	(0, 1/2, $z$ ), $z = 0.74154$
O 4k	( $x, 1/2, 1/2$ ), $x = 0.25375$
O 4m	( $x, 1/2, 0$ ), $x = 0.26$
O 2f	(1/2, 1/2, 1/4)

correct for the undefined nature of the long-range Coulomb interactions [49]. This correction requires knowledge of the high frequency electronic dielectric tensor  $\epsilon^\infty$  and Born effective charges  $\mathbf{Z}_i^*$ , where  $i$  labels each atomic site in the supercell. Both are obtained also using DFPT in response to a homogeneous electric field [46,50].

For calculations involving use of the VCA, we use the implementation in ABINIT. It is used to create an *alchemical* virtual atom of Ti/Zr character by linearly mixing the pseudopotentials of the individual species:

$$V_{\text{VCA}}^{\text{PS}} = xV_{\text{Zr}}^{\text{PS}} + (1-x)V_{\text{Ti}}^{\text{PS}}. \quad (1)$$

This can be further broken down into local contributions and short-range nonlocal corrections [51]. Phonon dispersion calculations using DFPT *and* the VCA are currently not fully supported in the code so we instead use the (formally equivalent) finite displacement method (FDM) as implemented in the Phonopy code (v2.1) [52] using a  $4 \times 4 \times 4$  supercell of the primitive perovskite unit and a displacement of 0.01 Å. For this calculation, the virtual atom must take on the intermediate mass of Ti and Zr, equal to 69.55 AMU. The NAC is accounted for following the same method as used in the DFPT calculations. For means of validation, a comparison of the phonon dispersions for PTO and PZO using both DFPT and the FDM are given in Sec. 2 of the Supplemental Material [53].

TABLE II. The diagonal elements of the stress tensor  $\sigma$ , high-frequency dielectric tensor  $\epsilon^\infty$ , and averaged born effective charges  $\bar{Z}^*$  of the unique elements for the primitive cubic perovskite following the convention of Ref. [48]. For PZT, these calculations were performed at  $a_{\text{Vg}}$  while PTO and PZO were performed at  $a_{\text{PTO}}$  and  $a_{\text{PZO}}$  respectively.

	$\sigma_{11}$ [GPa]	$\sigma_{22}$ [GPa]	$\sigma_{33}$ [GPa]	$\bar{Z}_{\text{Pb}}^*$	$\bar{Z}_{\text{B}}^*$	$\bar{Z}_{\text{O}\parallel}^*$	$\bar{Z}_{\text{O}\perp}^*$	$\epsilon_{11}^\infty$	$\epsilon_{22}^\infty$	$\epsilon_{33}^\infty$
PTO	$\approx 0$	$\approx 0$	$\approx 0$	3.88	7.19	-5.91	-2.58	8.49	8.49	8.49
PZO	$\approx 0$	$\approx 0$	$\approx 0$	3.90	5.94	-4.90	-2.47	6.93	6.93	6.93
Mean	$\approx 0$	$\approx 0$	$\approx 0$	3.89	6.55	-5.41	-2.53	7.71	7.71	7.71
VCA	-1.51	-1.51	-1.51	3.90	6.13	-4.99	-2.52	7.06	7.06	7.06
I	0.56	0.56	0.56	3.89	6.54	-5.36	-2.53	7.59	7.59	7.59
II	0.64	-1.60	0.64	3.89	6.55	-5.38	-2.53	7.59	7.67	7.59
III	-1.85	-1.85	0.50	3.86	6.48	-5.31	-2.51	7.54	7.54	7.52
IV	-0.67	-0.67	-0.67	3.87	6.49	-5.32	-2.52	7.55	7.55	7.55
V	-0.56	-0.56	0.59	3.88	6.53	-5.35	-2.53	7.60	7.60	7.57
VI	-0.62	-0.60	-0.60	3.87	6.51	-5.34	-2.52	7.56	7.57	7.57

For Sec. III B, we treat the six unique B-site configurations of  $\text{PbZr}_{0.5}\text{Ti}_{0.5}\text{O}_3$  within the  $2 \times 2 \times 2$  supercell labeled with Roman numerals I–VI. These supercells are shown in Fig. 1. Although PTO, PZO, and VCA calculations are representable in the primitive perovskite cell, we still choose to use the  $2 \times 2 \times 2$  supercell such that phonon dispersions are calculated along the same  $\mathbf{q}$  path as for structures I–VI and share the same total number of phonon branches ( $3 \times N_{\text{atom}} = 120$ ). PZT supercells are constrained to be cubic with dimensions  $(2a_{\text{Vg}}, 2a_{\text{Vg}}, 2a_{\text{Vg}})$ , where  $a_{\text{Vg}} = 4.029 \text{ \AA}$ , the lattice constant set by Vegard’s law [54]. For  $x = 0.5$ , this is a simple average of  $a_{\text{PTO}}$  and  $a_{\text{PZO}}$ . This choice of lattice constant favors no particular B-site ordering that may be biased in different experimental conditions. Further, structural data for high-temperature cubic PZT is scarce since the technologically relevant large piezoelectric coefficients stem from the low-temperature tetragonal/rhombohedral phases. Simulations for PTO and PZO are performed at their theoretical lattice constants. Before the phonon calculations, internal degrees of freedom are relaxed to a stringent force tolerance of  $1 \times 10^{-6} \text{ eV/\AA}$  to prevent soft modes forming from nonequilibrium vibrations. To further illuminate the mode characters, we also calculate the phonon PDOS for each structure. To do so, we calculate the dynamical matrix on a dense  $49 \times 49 \times 49$  grid of  $\mathbf{q}$  points and integrate with the tetrahedron method [55].

Throughout this work, we make use of group theoretical software. We use the programs FINDSYM (v6.0) [56] and ISODISTORT (v6.5) [57] as made available in the ISOTROPY software suite. We also make use of the web-based phonon spectrum visualization tools made available by Miranda [58].

### III. RESULTS

#### A. Parent structures

Table I details the structural and symmetry properties of the relaxed primitive cells. We find that a simple metric like the number of Wyckoff sites (and their deviation from the ideal perovskite sites) suggests which arrangements have comparable lattice dynamics. This is used as a basis for the discussion in Sec. III B. These primitive cells are then translated into the  $2 \times 2 \times 2$  supercell of the primitive  $\text{PbBO}_3$  unit ( $\text{B} = \text{Zr}$  or  $\text{B} = \text{Ti}$ ) and are shown in Fig. 1. These form a

set of parent structures from which we later perform mode decomposition analysis. Table II shows other important structural, dynamical, and dielectric properties also important to the discussion in this section.

PTO/PZO/VCA cells show the usual cubic  $Pm\bar{3}m$  symmetry. These are joined by PZT I ( $Fm\bar{3}m$ ) and IV ( $Pm\bar{3}m$ ) which also support a cubic local minimum. The former adopts rock-salt-like ordering with continuous B sites aligned along the [111] direction while the latter shows a separation of Ti and Zr sites into opposite corners of the supercell. As a consequence, these parents show isotropic behavior in both the stress and high-frequency dielectric tensor (Table II). This is in contrast to the other four PZT parents which are members of lower symmetry tetragonal space groups (even while constrained to  $a_{\text{Vg}}$ ), thus showing anisotropic behavior in these tensors about a single axis. It is typical behavior across all of the PZT parents (bar the VCA) to compress areas of  $\text{TiO}_6$  coordination, making way for the larger  $\text{ZrO}_6$  octahedra. When constrained to  $a_{\text{Vg}}$ , PZT I is the most energetically stable configuration while III is the most unstable, with an energy difference of 114 meV/ $\text{PbBO}_3$  unit between them. Remarkably, if we perform a full cell shape and size relaxation, this energy difference marginally narrows to 111 meV/ $\text{PbBO}_3$ , showing the small contribution of strain energy to the nonpolar phases of PZT.

Table II indicates that at  $a_{\text{Vg}}$ , PZT is held at a nonvanishing pressure. The VCA exhibits the largest  $\sigma_{\text{RMS}}$  of 2.62 GPa while II and III show stronger uniaxial stress about the axes of compositional modulation, indicating a proclivity for expansion in these directions. PZT I–VI show remarkably similar  $\mathbf{Z}^*$  and  $\epsilon^\infty$ , indicating that Ti/Zr cation ordering has little influence on these quantities. It is also notable that  $\mathbf{Z}^*$  of PZT I–VI deviates only a small amount from the mean  $\mathbf{Z}^*$  of PZO and PTO. The VCA shows good agreement with the supercell method for  $\bar{Z}_{\text{Pb}}^*$  and  $\bar{Z}_{\text{O}\perp}^*$  but underestimates strongly the magnitudes of the alchemical  $\bar{Z}_{\text{B}}^*$  and  $\bar{Z}_{\text{O}\parallel}^*$ . The VCA also features a strong discrepancy in  $\epsilon^\infty$  compared to both the mean and supercell approach. Although not tabulated, it should be noted that PZT II, IV, V, and VI feature off-diagonal elements in the Born effective charge tensor only for  $\bar{Z}_{\text{Pb}}^*$ . These components are small and do not exceed 0.34

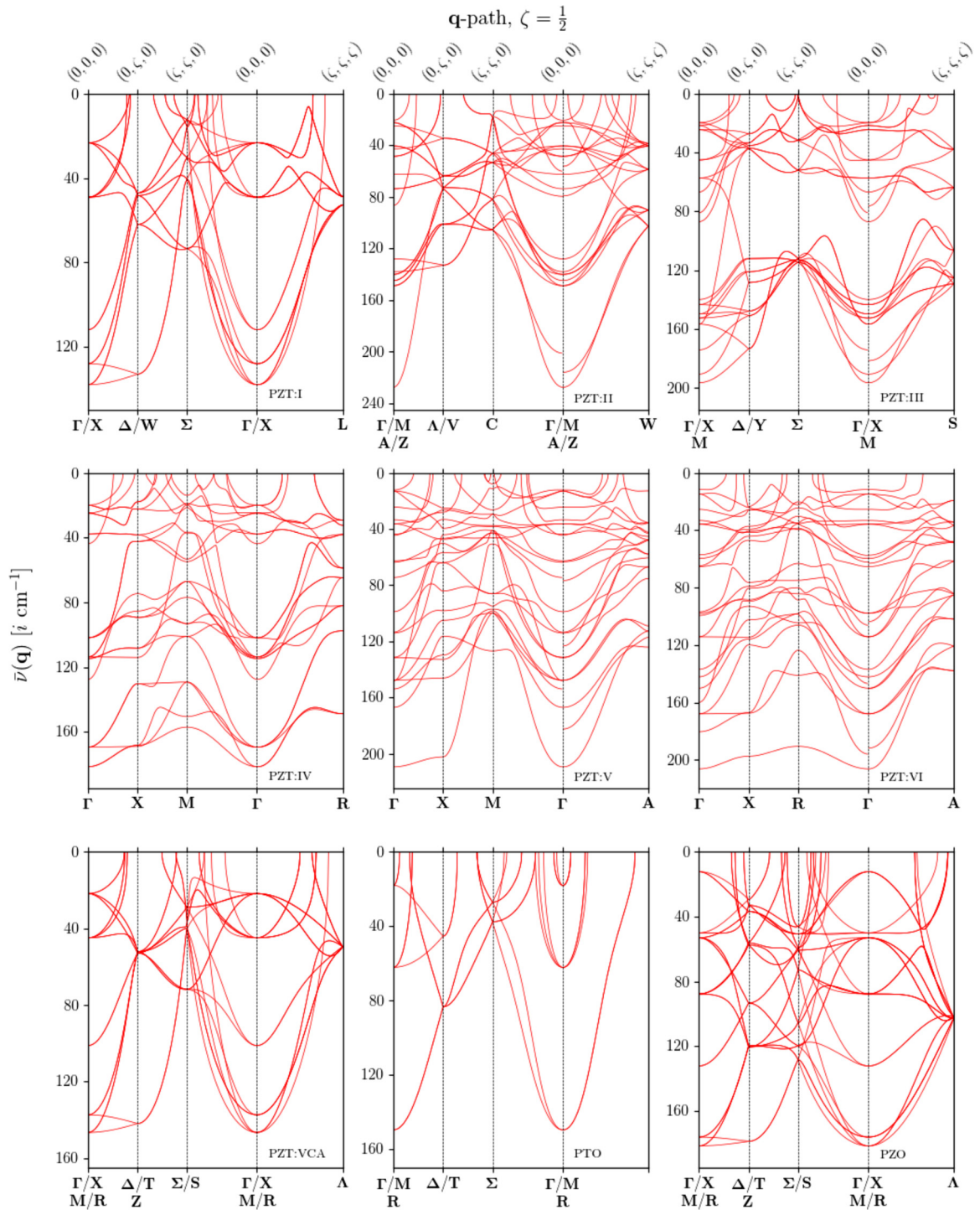


FIG. 2. The soft mode phonon dispersion relations for PZT I–VI, the VCA, PTO, and PZO. All dispersions are over an identical fractional  $\mathbf{q}$  path controlled by the parameter  $\zeta = 1/2$  (upper  $x$  axis). Folded symmetry labels (described in Table III) are included for PZT I–III, the VCA, PTO, and PZO. We only include folded labels if a soft mode of that wave vector is present at the given  $\mathbf{q}$  point. In the particular case of PTO, this leads to no label for the wave vector  $(1/2, 1/2, 1/2)$ . Since dispersions for PZT IV–VI were calculated on the primitive cell, no folding takes place and thus only one symmetry label is required.

electronic charges in magnitude but do vary in sign despite the positive nature of the Pb cation. It should also be noted that using a similar method, a previous study reports off-diagonal elements not of Pb, but of the O 4k site, always negative in sign [28].

### B. Phonon dispersion and density of states

Figure 2 shows the phonon dispersions for PZT I–VI, PTO, PZO, and the VCA calculated within the supercells indicated in Fig. 1. Although we have calculated all bands

TABLE III. The fractional  $\mathbf{q}$  vectors associated with the Brillouin zone labels used in Fig. 2. For each space group, labels in bold indicate high symmetry points while those in plain font are not special points. For the full Brillouin zone vector identification, the reader is referred to the database made available by the Bilbao Crystallographic Server [62].

$(q_x, q_y, q_z)$		$(q_x, q_y, q_z)$	
<b><i>Pm</i><math>\bar{3}m</math> <math>O_h^1</math></b>			
<b><math>\Gamma</math></b>	(0, 0, 0)	<b><math>R</math></b>	(1/2, 1/2, 1/2)
<b><math>X</math></b>	(0, 1/2, 0)	$\Delta$	(0, 1/4, 0)
<b><math>M</math></b>	(1/2, 1/2, 0)	$T$	(1/2, 1/2, 1/4)
$Z$	(1/4, 1/2, 0)	$\Sigma$	(1/4, 1/4, 0)
$S$	(1/4, 1/2, 1/4)	$\Lambda$	(1/4, 1/4, 1/4)
<b><i>Fm</i><math>\bar{3}m</math> <math>O_h^5</math></b>			
<b><math>\Gamma</math></b>	(0, 0, 0)	<b><math>W</math></b>	(1/2, 1/4, 3/4)
<b><math>X</math></b>	(1/2, 0, 1/2)	$\Sigma$	(1/4, 1/4, 1/2)
$\Delta$	(1/4, 0, 1/4)	<b><math>L</math></b>	(1/2, 1/2, 1/2)
<b><i>P4</i>/<i>mmm</i> <math>D_{4h}^1</math></b>			
<b><math>\Gamma</math></b>	(0, 0, 0)	$C$	(1/4, 1/4, 1/4)
<b><math>X</math></b>	(0, 1/2, 0)	$V$	(1/2, 1/2, 1/4)
<b><math>M</math></b>	(1/2, 1/2, 0)	$W$	(0, 1/2, 1/4)
<b><math>A</math></b>	(1/2, 1/2, 1/2)	$\Delta$	(0, 1/4, 0)
<b><math>Z</math></b>	(0, 0, 1/2)	$Y$	(1/4, 1/2, 0)
$\Lambda$	(0, 0, 1/4)	$\Sigma$	(1/4, 1/4, 0)
$S$	(1/4, 1/4, 1/2)		
<b><i>P4</i><sub>2</sub>/<i>mmc</i> <math>D_{4h}^9</math></b>			
<b><math>\Gamma</math></b>	(0, 0, 0)	<b><math>X</math></b>	(0, 1/2, 0)
<b><math>R</math></b>	(0, 1/2, 1/2)	<b><math>A</math></b>	(1/2, 1/2, 1/2)

(available in Sec. 3 of the Supplemental Material [53]), we consider only the space where  $\bar{\nu}(\mathbf{q}) \in i\mathbb{R}$ , thus presenting a set of symmetry-lowering phase transitions along the fractional  $\mathbf{q}$  path  $(0, 0, 0) \Rightarrow (0, 1/2, 0) \Rightarrow (1/2, 1/2, 0) \Rightarrow (0, 0, 0) \Rightarrow (1/2, 1/2, 1/2)$ . It is at these supercell wave vectors exactly that we analyze the character of the distortions. The soft-mode character has an important impact on the properties of the crystal. This is then inferred with PDOS calculations (Figs. 4 and 5) and, for some important modes, found directly with eigendisplacement analysis. Table IV serves as a companion to the dispersion, identifying modes symmetries, their multiplicities, and numerical values of imaginary frequencies. Table III presents the  $q$ -vectors associated with the high-symmetry labels which also serves as a companion to Fig. 2.

### 1. PTO and PZO

We begin with a discussion of end members PTO and PZO. Our choice of supercell for these calculations reveals folded spectra not previously reported in the literature. We have also, however, calculated dispersions over the primitive cell and found good agreement with previous calculations using similar methods [43,60] (see Sec. 2 of the Supplemental Material [53]). For PTO, we report seven unique soft modes at the appropriate wave vectors compared to 26 in the more complex spectrum of PZO. As expected, the most unstable mode in PTO is found to be  $\Gamma_4^-$ , featuring Pb/Ti counter-motion

against the O anions, inducing a net polarization and incipient FE distortion. Although the  $\Gamma_4^-$  distortion exists in PZO, it is harder and features Zr motion *alongside* O, requiring that the smaller macroscopic polarization is as the result of Pb-O separation. PTO shows oxygen octahedron rotational instabilities at the R and M points. These are the  $R_4^+$  and  $M_3^+$  AFD modes respectively. In real space, these correspond to out-of-phase and in-phase rotations of the  $BO_6$  octahedra about a single axis, or  $a^0a^0c^-$  and  $a^0a^0c^+$  in Glazer's notation, respectively. These modes are generally not competitive in PTO but this is *not* true for PZO. The  $R_4^+$  distortion is the softest mode in PZO and is a prime mover for the AFE phase transition, known to make up  $\approx 60\%$  of the total distortion [61] (when the rotation is about the  $[1\bar{1}0]$  axis).

Branches mostly harden along the  $(0, 0, 0) \Rightarrow (0, 1/2, 0)$  path in PTO, resulting in an antipolar mode  $\Delta_5$  and a long wavelength AFD mode  $T_4$ . The latter shares a likeness with both  $a^0a^0c^-$  and  $a^0a^0c^+$  distortions but with a doubled periodicity of four perovskite units along the axis of rotation. Of the four  $TiO_6$  octahedra in the mode, two neighboring octahedra rotate counterclockwise and the other two clockwise about the axis of rotation as seen in Fig. 3(i) (left). Although there is also a general hardening of branches along the same path in PZO, the softest is almost dispersionless, resulting in another AFD mode of symmetry  $T_4$ . Although over the same wave vector as the  $T_4$  mode of PTO, this mode is better described as an  $a^0a^0c^-$ -like distortion where rotating octahedra are separated by static ones [Fig. 3(i) (right)]. Both PTO and PZO now become harder at  $(1/2, 1/2, 0)$ , resulting in several antipolar modes and, for the first time in this study, single modes with a mixed antipolar/AFD character. These modes often manifest in a sublattice of  $BO_6$  octahedra rotating with a Glazer-like pattern with adjacent  $PbBO_3$  units, showing local polar distortions. These local polar distortions are aligned such that there is no net polarization induced by the mode. An example of this is the  $\Sigma_2$  distortion of PTO, although it has relatively low soft-mode frequency ( $27.05i$   $cm^{-1}$ ). Modes of this character are considerably softer in PZO, including the  $S_4$  distortion, which features local AFD modes (with a complex non-Glazer-like rotation pattern) and antipolar cation displacements. This mode is also known to make a small contribution to the AFE PZO ground state [61].

Along the  $(0, 0, 0) \Rightarrow (1/2, 1/2, 1/2)$  path, the dispersion now becomes real in PTO and thus we see no instabilities at this longer wavelength. For PZO, the dispersion remains imaginary. We see a hardening resulting in two strongly degenerate modes of symmetry  $\Lambda_2$  and  $\Lambda_3$ . The former is an eight-fold degenerate AFD mode while the latter is 16-fold degenerate, featuring Pb-O antipolar displacements. The character of these modes are reminiscent of some of the known modes contributing to the PZO ground state. This suggests that the inclusion of these distortions, with others, could create another similar low-energy competing phase. Figure 4 shows that the two end members have a striking dissimilarity in the PDOS. All species for PTO show a rather featureless smooth function, peaking at  $\approx 24i$   $cm^{-1}$  while PZO shows a peaked PDOS penetrating further into the imaginary space, indicating that cubic PZO is more dynamically unstable than PTO. The peak at  $\approx 50i$   $cm^{-1}$  is in part due to the dispersionless behavior of a Pb-O antipolar branch extending from  $(1/2, 1/2, 0) \Rightarrow$

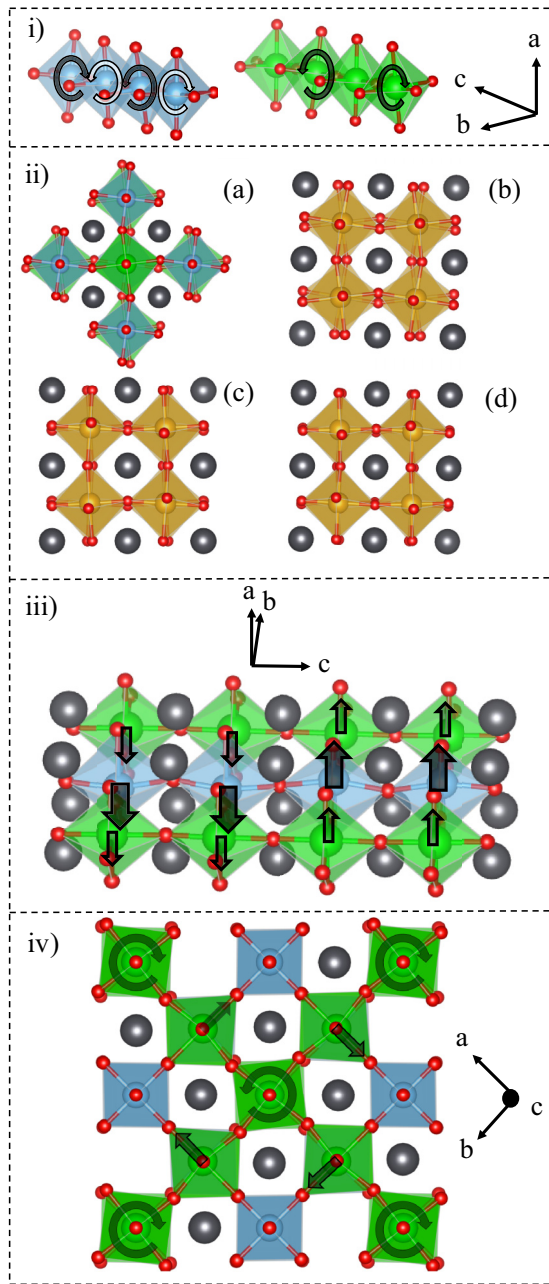


FIG. 3. Visualization of eigendisplacements described in the text following the same key as Fig. 1 but also with gray spheres representing Pb sites. (i) The  $T_4$  modes of PTO and PZO. Both Pb and counter-rotating octahedra are removed for clarity. (ii) The  $\Gamma_4^+$  distortion of PZT I ( $c$  axes into page) and the  $M_2^+$  distortion of the VCA from three viewing angles indicating out-of-phase rotation about three axes of rotation. (iii) The antipolar  $\Delta_4$  distortion of PZT III. Arrows indicate the direction and magnitude of the local polarization. (iv) The mixed antipolar/AFD  $M_3^+$  distortion of PZT IV.

$(0, 0, 0)$ . This behavior continues for most of the  $(0, 0, 0) \Rightarrow (1/2, 1/2, 1/2)$  path also. It is noteworthy that the Pb character vanishes for the softest part of the PZO PDOS, leaving just modes of Zr-O character.

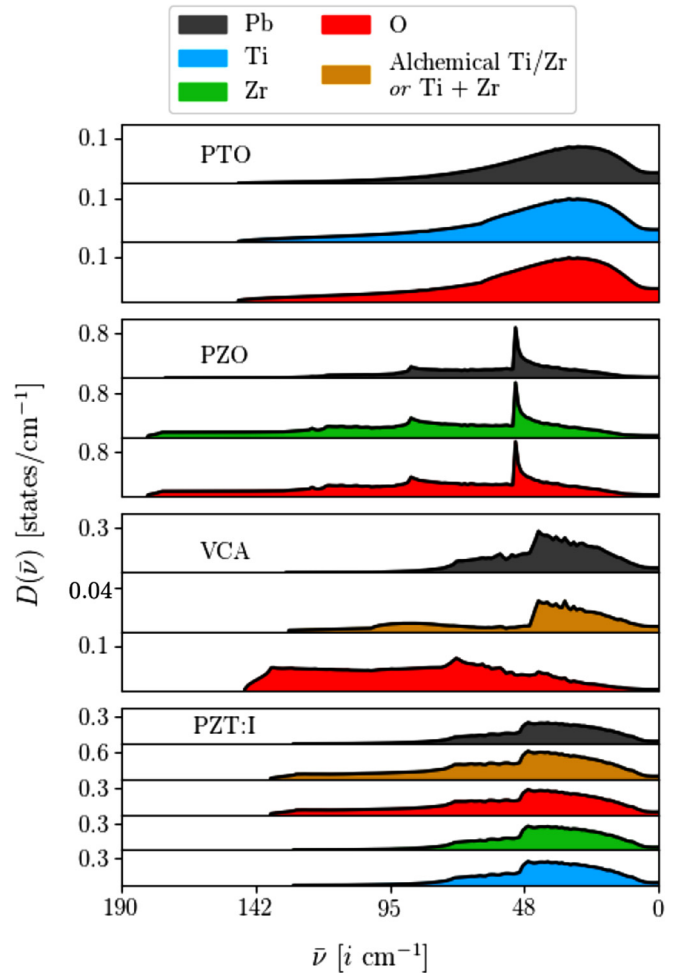


FIG. 4. Species projected phonon density of states  $D(\bar{\nu})$  for PTO, PZO, the VCA, and PZT I over the imaginary wave-number space. For the VCA calculation, the gold curve is the PDOS of the alchemical 50/50 Ti/Zr atom while for the supercell models it represents the sum of B-site PDOS.

## 2. Virtual crystal approximation and PZT I

There is a remarkable visual similarity in the dispersion relations between PZT I and the VCA. At first glance, this suggests that within the mixed potential scheme the dynamics of alternating Zr and Ti atoms in the rock-salt structure are well approximated. We do, however, see more unique branches for PZT I and find that the lowest lying modes of the VCA penetrate further into the soft space than its rock-salt ordered counterpart. It is also true that both approaches resemble PZO more so than PTO. This can be seen when assessing the modes at wave vector  $(0, 0, 0)$ . At this point, PZT I, the VCA, and PZO share a similar hierarchy of modes. PZT I and the VCA also share identical multiplicities. In descending order in imaginary wave number, we have out-of-phase AFD, in-phase AFD, FE, and then a number of antipolar modes. It is illuminating in this case to perform a full analysis of the character. It soon becomes apparent that the VCA features AFD modes about all three axes of rotation. The amplitude of these rotations about two of the axes is small and much larger for the remaining axis. We

could then consider these modes as rotations about a single axis but with small, erroneous rotations about the other axes. This is in contrast to PZT I where the softest AFD mode ( $\Gamma_4^+$ ) has (like both end members) an  $a^0a^0c^-$  displacement pattern, shown in Fig. 3(ii)(a). In the VCA, this rotation ( $M_2^+$ ) retains its out-of-phase characteristic but now rotates about all three axes of rotation with different amplitudes, thus exhibiting the  $a^-b^-c^-$  rotation pattern shown in Figs. 3(ii)(b) and 3(ii)(d). The next softest mode in PZT I ( $X_3^+$ ) has the  $a^0a^0c^+$  pattern while the in-phase rotations in the VCA ( $R_5^-$ ), as before, have differing amplitudes about all three axes of rotations. This is the  $a^+b^+c^+$  rotation pattern. The rotation patterns in the VCA are *not* seen in any of the PZT supercell models, indicating that rotations about more than one axis are a fictitious artifact of the method, better illustrating the inaccuracy of the VCA in the prediction of local atomic displacements.

The character of the FE  $\Gamma_4^-$  modes are also dissimilar in nature. For PZT I, all ions play a role in the development of polarization, including Ti and Zr displacement of a similar magnitude. For the VCA, the alchemical B site plays much less of a role. We can then infer (without the full Berry-phase calculation) that the incipient polarization is smaller in magnitude in part owed to the smaller B-site displacements but also due to the smaller value of  $\bar{Z}_B^*$  (Table II). A lack of alchemical B-site character is in fact commonplace for the VCA, as evidenced in Fig. 4, where although optically coupled to Pb motion, it has an almost vanishingly small PDOS. This suggests that within the VCA, the B site is dynamically inert. This leaves the softest modes of the VCA to have nearly a pure O character. It is only for Pb that we see similarity in the PDOS between the VCA and PZT I. We see a peak in the Pb  $D(\bar{\nu})$  for PZT I at  $\approx 48i \text{ cm}^{-1}$ , which is shifted  $\approx -2i \text{ cm}^{-1}$  in the VCA. The Pb peak in PZT I coincides with the other species. Such a coupling is in fact true for all PZT configurations and end members PTO/PZO. It is unique to the VCA that we see little coupling between Pb and O. This can be regarded as a knock-on effect of the inert B site. Since Pb and B-site vibrations are weakly coupled, the usual B-site displacements which would otherwise follow Pb are not present. It is these displacements which more greatly influence O motion since Pb has only a weaker mixed ionic/covalent interaction with O. While we expect the general fictitious character of the eigendisplacements to persist across all concentrations within the VCA, it is likely that the magnitude of the error may vary. We expect largely fictitious eigendisplacements when Ti/Zr concentrations are comparable but expect the effect to diminish in the limit of high/low concentrations where the mixed potential becomes very similar to the original, unmixed pseudopotential.

Moving away from (0, 0, 0) toward (0, 1/2, 0) both PZT I and the VCA give rise to longer wavelength AFD and antipolar modes. The  $T_2$  and  $\Delta_4$  modes of the VCA and PZT I, respectively, display the same rotation pattern as the aforementioned  $T_4$  distortion in PTO. This mode is significantly more unstable in PZT I. Despite the VCA appearing to have a higher degeneracy for the antipolar soft modes at  $\approx 50i \text{ cm}^{-1}$ , modes are still unique splitting only by  $\approx 0.5i \text{ cm}^{-1}$ . One of these modes,  $Z_1$ , is not purely antipolar and once again we see the mixed AFD/antipolar character displaying non-Glazer-like rotations coupled with Pb cation motion.

Like PZO, both the VCA and PZT I become their hardest along the (0, 1/2, 0)  $\Rightarrow$  (1/2, 1/2, 0) path. This leads to further antipolar modes at the  $\Sigma$  and S points. Notably, PZT I gains an additional soft mode from the real domain along this path,  $\Sigma_1$ . This is distinct from the other Pb-O modes since it features antipolar Pb-B displacements with no significant O character. For the VCA, there is also a fourfold degenerate mode  $Z_1$  once again with mixed antipolar/AFD character. The most distinct differences in the dynamical behavior between the VCA and PZT I now comes along the path (0, 0, 0)  $\Rightarrow$  (1/2, 1/2, 1/2). Many of the harder antipolar branches in the VCA move to the real domain. These modes do begin to harden in PZT I but then soften to become degenerate with other branches at the L point, giving rise to two long-wavelength modes both of symmetry  $L_3^-$ . Now commonplace, they share a mixed antipolar/AFD character split by  $\Delta\bar{\nu} = 4.13i \text{ cm}^{-1}$ . We distinguish between modes sharing an irrep by priming those with the lower imaginary frequency, as seen in Table IV. Each mode has eight-fold degeneracy despite  $L_3^-$  having a longer wavelength AFD rotation pattern than  $L_3^-$ . This splitting closes for the VCA, giving rise to one 16-fold degenerate mode of symmetry  $\Lambda_3$  displaying a similar mixed antipolar/AFD character.

### 3. PZT II and III

We move now to consider the dispersions of PZT II and III. These are the [110] and [001] ordered superlattices respectively. These structures were considered in a previous work in a study of the instabilities at the  $\Gamma$  point [28] using the local density approximation (LDA). Consistent with the previous work, we find that both PZT II and III have strong TO FE instabilities of  $\Gamma_3^-$  and  $\Gamma_5^-$  symmetry respectively. The softest TO mode of the [110] ordered structure is not seen in our dispersion path due to the anisotropy of LO-TO splitting in noncubic crystals. This anisotropy can be reasoned by the form of the NAC. Recall that the NAC is a function of both  $Z_i^*$  and  $\epsilon^\infty$ . The former gains more unique elements in lower symmetry crystals and the latter is no longer isotropic, as evidenced in Table II. The affected elements of the dynamical matrix are then corrected by a different amount based on the direction of the  $\mathbf{q}$  vector as it approaches  $\Gamma$ . This effect is seen in PZT II, II, V, and VI since they are all members of a tetragonal spacegroup. These anisotropies are also accessible in experiments as evidenced by inelastic neutron scattering in tetragonal PTO [63]. Taking just the analytic part of the  $\Gamma_3^-$  mode of PZT II returns an eigenfrequency of  $242.28i \text{ cm}^{-1}$ , slightly softer than what is predicted by the LDA.

We find that both PZT II and III give rise to soft LO modes, again, in agreement with the previous work. The [110] ordering is generally more dynamically unstable than [001] ordering, showing a distinct separation between the most imaginary FE/antipolar modes and groupings of Glazer AFD modes. What was not considered in a previous study [28] was competition of polar modes with other order parameters. The antipolar mode  $M_3^-$  of PZT II is closely competitive with  $\Gamma_5^-$ . This mode is an antipolar arrangement of Ti-O displacements completely isolated to local PTO environments, leaving undistorted areas of PZO units. There are also a plethora of unique Glazer tilt modes owed to inequivalent directions in



TABLE IV. The ten softest modes, for each structure, measured along the phonon dispersion path in Fig. 2 (with the exception of PTO, featuring only seven soft-modes over the dispersion path). Modes are listed in descending imaginary wave number  $\bar{\nu}$  across the page. Each entry features a symmetry label for the irrep and a multiplicity  $M$ . Since PZT II–IV and VI feature directional polar modes, affected wave numbers are given in the format  $\bar{\nu}_{[010]}/\bar{\nu}_{[110]}/\bar{\nu}_{[111]}$ . The full tabulation of all soft modes can be found in Sec. 1 of the Supplemental Material [53].

		$M$	$\bar{\nu}$ [ $i$ cm $^{-1}$ ]		$M$	$\bar{\nu}$ [ $i$ cm $^{-1}$ ]		$M$	$\bar{\nu}$ [ $i$ cm $^{-1}$ ]
PTO	$\Gamma_4^-$	2	149.60	$\Delta_5^+$	4	83.40	$R_4^+$	3	62.12
	$T_4$	2	45.40	$\Sigma_3$	4	37.61	$\Sigma_2$	4	27.05
	$M_3^+$	3	18.02						
PZO	$R_4^+$	3	181.52	$T_4$	2	178.75	$M_3^+$	3	176.09
	$\Gamma_4^-$	2	132.14	$S_4$	4	128.32	$T_5$	4	120.45
	$\Sigma_2$	4	119.69	$Z_4$	4	119.53	$S_3$	4	105.37
	$\Lambda_2$	8	103.13						
VCA	$M_2^+$	3	146.58	$\Delta_5$	2	141.95	$R_5^-$	3	137.38
	$\Gamma_4^-$	2	101.18	$S_1$	4	71.78	$T_2$	4	52.87
	$Z_1$	4	52.18	$T_5$	4	52.14	$\Lambda_3$	16	49.55
	$X_5^-$	6	44.89						
I	$\Gamma_4^+$	3	138.10	$\Delta_4$	2	133.08	$X_3^+$	3	128.11
	$\Gamma_4^-$	2	111.99	$\Sigma_2$	4	73.53	$\Delta_5$	4	62.02
	$L_3^-$	8	52.83	$X_5^-$	6	49.09	$L_3^-'$	8	48.70
	$W_5$	4	48.29						
II	$M_3^-$	1	227.52	$\Gamma_5^-$	1	144.78/201.13/215.93	$Z_5^-$	2	148.78
	$A_5^-$	2	140.02	$Z_1^-$	1	137.91	$\Lambda_4$	2	132.92
	$\Gamma_3^+$	1	127.97	$C_1$	4	105.26	$\Lambda_5$	4	101.14
	$W_2$	4	90.22						
III	$\Gamma_5^-$	1	196.63/196.63/196.63	$M_2^+$	1	190.76	$\Gamma_3^-$	1	174.29/174.29/181.62
	$\Delta_4$	2	173.52	$X_2^+$	2	156.67	$M_5^+$	2	152.61
	$\Delta_3$	2	150.97	$X_3^+$	2	149.79	$Y_3$	2	147.85
	$X_2^-$	2	143.46						
IV	$\Gamma_4^-$	2	181.41	$\Gamma_4^+$	3	169.33	$X_3^+$	1	168.90
	$X_5^+$	2	168.18	$M_2^-$	1	157.00	$M_3^+$	1	150.48
	$R_4^+$	3	148.69	$X_5^{+'}$	2	130.13	$M_5^+$	2	129.20
	$\Gamma_4^-'$	2	114.61						
V	$\Gamma_5^-$	1	209.42/209.42/209.42	$X_3^-$	1	202.33	$\Gamma_3^-$	1	153.93/153.93/182.48
	$\Gamma_3^+$	1	167.07	$\Gamma_5^-'$	1	148.18/148.18/123.20	$\Gamma_5^+$	1	147.67
	$X_4^+$	1	146.16	$X_1^-$	1	132.83	$\Gamma_5^{+'}$	2	131.48
	$X_2^-$	1	129.84						
VI	$\Gamma_5^-$	1	206.22/206.22/206.22	$X_2^+$	1	197.36	$\Gamma_3^-$	1	180.33/195.87/191.69
	$R_1^-$	1	190.45	$\Gamma_5^+$	2	167.85	$X_4^+$	1	167.42
	$X_3^+$	1	167.00	$\Gamma_5^-'$	1	159.78/146.71/150.21	$\Gamma_4^+$	1	149.99
	$\Gamma_3^+$	1	142.07						

the crystals and thus inequivalent axes of rotation. The softest of these is an  $a^0a^0c^-$  mode with the axes of rotation along the [001] (or [010]) direction, the direction of compositional modulation. This is followed by a several antipolar modes and harder FE modes. In PZT III, rotational instability is highly competitive with FE order due to the  $M_2^+$  mode. This mode shows in-phase rotation of  $ZrO_6$  octahedra, leaving the  $TiO_6$  octahedra static in a manner reminiscent of the  $T_4$  distortion of PZO. This shows there is no mechanical coupling along the axis of rotation between octahedra centered on a different B-site species. While rotations of all octahedra are also unstable (both out-of-phase  $M_5^+$  and in-phase  $X_2^-$ ), they are harder. Further, both of these modes rotate along homogeneous B-site chains, whereas the  $M_2^+$  mode rotates along the heterogeneous direction where no other Glazer-type instability exists.

The character of AFD modes in PZT II alters as we approach the wave vector  $(0, 1/2, 0)$ . This mode shows out-of-phase rotations of the  $ZrO_6$  octahedra but with a doubled periodicity. Rotating octahedra are also separated by static  $ZrO_6$  octahedra, this time showing a lack of interlayer coupling even along the homogeneous direction. A long-wavelength AFD mode also exists for PZT III at this wave vector of irrep  $Y_3$ . This mode shows the same character of the  $T_4$  mode of PTO with the axis of rotation being along the homogeneous direction. This wave vector for PZT III, however, is dominated by antipolar instability with the most unstable being the  $\Delta_4$  mode. This mode appears with two separate polar domains with a domain period of 4 perovskite units, separated by a  $180^\circ$  domain wall as depicted in Fig. 3(iii). Local PTO units are significantly more polar than local PZO units.

Like in PZT I, the VCA, PTO, and PZO, the most imaginary bands at  $(0, 1/2, 0)$  have a steep gradient to the hard wave vector  $(1/2, 1/2, 0)$ . This results in tight groupings of antipolar and mixed antipolar/AFD modes for PZT III but only antipolar modes for PZT II. The dispersion now returns to  $(0, 0, 0)$ . We note that along this direction of approach ( $[110]$ ), anisotropy in LO-TO splitting allows for softer LO FE modes to appear in both PZT II and III and softer still along the  $[111]$  direction. This results in sharp discontinuities in the spectra. From  $(0, 0, 0)$  to the long wavelength  $(1/2, 1/2, 1/2)$  point, hardening occurs for both PZT II and III, giving rise to five distinct distortions for each arrangement. For PZT II, these are the  $W_{1-4}$  (where the subscript indicates all modes with integers 1 through 4) and  $W'_1$  distortions. Each of these modes has a pure antipolar character. Further, the splitting of the isosymmetrical modes  $W_1$  and  $W'_1$  is large ( $64.16i \text{ cm}^{-1}$ ) due to the inclusion of Zr displacement in  $W'_1$  where  $W_1$  features static Zr. PZT III possesses similar characteristics in its long wavelength distortions,  $S_{1-4}$  and  $S'_4$ . Unlike PZT II, two of these distortions have the mixed AFD/antipolar character while the remaining are purely antipolar. The  $S_4$ - $S'_4$  splitting is also large ( $61.19i \text{ cm}^{-1}$ ) but is now the result of the inclusion of local AFD displacements in  $S_4$  while  $S'_4$  is purely antipolar.

The general character of the distortions in both PZT II and III can be inferred from the PDOS (Fig. 5). We see that for both arrangements, all species are optically coupled to one another, but, like before, the Pb character starts to diminish as we penetrate further into the soft domain. While both PZT II and III give rise to two separated islands of states in the PDOS, a sharp peak exists on the softer island of PZT II at  $\approx 100i \text{ cm}^{-1}$ . This is owing to the nearly dispersionless behavior of the antipolar branch connecting the  $\Lambda_5$  and  $C_1$  modes. The fourfold degenerate  $W_1$  antipolar mode also appears at this wave number (along with  $\Lambda_5$  and  $C_1$ ) containing significant Pb character.

#### 4. PZT IV

We discuss now PZT IV in isolation, which, despite sharing  $m\bar{3}m$  symmetry with PZT I, shows radically different dynamical behavior as well as being generally more unstable. For the first time in this study, also, we consider dispersion over what is the primitive lattice so we pass through high-symmetry points without any folding of the BZ. Unlike PZT I, the softest mode at  $(0, 0, 0)$  is now a  $\Gamma_4^-$  distortion, which suggests but does not guarantee a FE ground state. This is because the phonon frequency gives us only information on the instability of the mode and *not* on the magnitude of energy lowering once the soft lattice mode has condensed in the crystal. This distortion shows stronger local polarity in directions with continuous PTO units. The presence of Zr along a polar direction dampens the distortion. For the first time in this study, no pure Glazer type AFD instabilities are found to exist in a single mode. These are replaced with isolated in-phase AFD instabilities, the softest of which is the  $\Gamma_4^+$  mode. This mode features a rotating layer (isolated by static  $\text{PbBO}_3$  layers) with a ratio of 8:1  $\text{ZrO}_6$  to  $\text{TiO}_6$  octahedra. In this case, the dominance of the PZO-rich environment (which favors rotation) is able to overpower the single PTO unit (favoring FE distortion) into

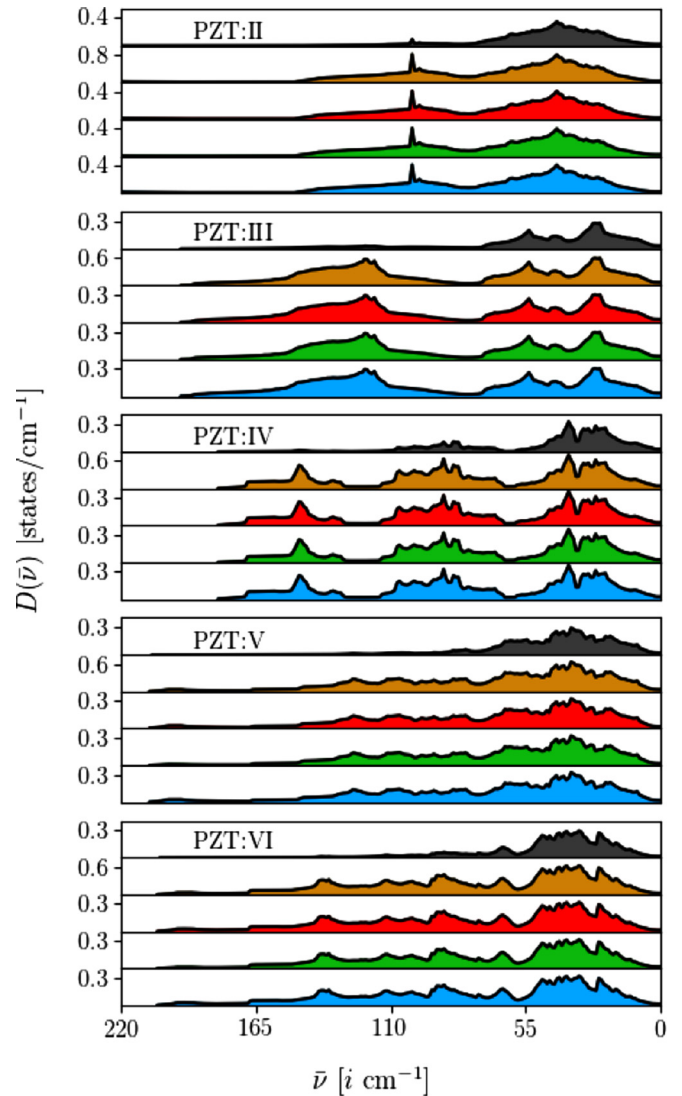


FIG. 5. Species projected phonon density of states  $D(\bar{\nu})$  for PZT III–VI over the imaginary wave-number space. This figure shares a legend with Fig. 4.

rotation. One other rotational instability exists at this point,  $\Gamma_4^{+'}$ . This mode shares the same characteristics as  $\Gamma_4^+$ , but the rotating layer contains fewer  $\text{ZrO}_6$  octahedra, making the mode more stable than its counterpart. It is notable that there are three separate occurrences of the FE  $\Gamma_4^-$  irrep:  $\Gamma_4^-$ ,  $\Gamma_4^{-'}$ , and  $\Gamma_4^{-''}$ . The latter (although much harder than the others) is distinct not only due to its weak B-site displacements but also to its alternating Pb cation motion transverse to the direction of polarization, giving rise to a mode of a mixed FE and antipolar character at the zone center.

Most bands harden only slightly along the path to X, much in contrast to the superlattice-type arrangements. Antipolar-type distortions at this wave vector are much harder than previous arrangements featuring only Pb-O motion. There is now only a slight hardening in the dispersion along the  $\Gamma \Rightarrow X$  path, once again leading to a selection of antipolar and AFD modes. The  $X_3^+$  and  $X_5^+$  modes are particularly unstable. The first is a long-wavelength AFD mode much like  $\Gamma_4^+$  but with out-of-phase rotations. These rotational modes are very

closely competing split by  $<1i \text{ cm}^{-1}$  in the favor of  $X_3^+$ . The second,  $X_5^+$ , is an isolated antipolar distortion where local PTO units are polar in the direction of compositional homogeneity. PZO units are once again resistant to polarization and are left static. After a small degree of hardening along the path to M, we find 15 unique distortions of antipolar and mixed AFD/antipolar character, the largest concentration of such states in this study. The softest is antipolar  $M_2^-$ , bearing great resemblance to  $X_5^+$  but over a greater wavelength.

The  $M_3^+$  mode is the clearest example of a mixed AFD/antipolar mode. This is shown in Fig. 3(iv). It features a central in-phase rotation similar to  $\Gamma_4^+$ .  $\text{PbBO}_3$  units perpendicular to the axis of rotation now show local polar displacements in a pattern enclosing the central rotating unit. Softer modes of this character can be seen at the R point. Here we find that the most unstable branches are dominated by the mixed AFD/antipolar character. In fact, the unstable mode of this character, among all PZT arrangements, is found here and is the triply degenerate  $R_4^+$ . This shares great similarity to  $M_3^+$  but rotations are out of phase and about two axes, making the rotation pattern  $a^0b^-b^-$ -like. Other modes at this wave vector are also visually similar to  $M_3^+$  but now the local polar regions include Pb and Ti cation motion where before local polarity was just as the result of O displacing against static Zr.

PZT IV is the only arrangement to form three distinct islands in the PDOS. The two more stable islands feature coupled ionic motion between all species, but as before the most imaginary states have a diminished Pb character. It is clear that the first (and least imaginary) island is composed entirely of antipolar states and the second of antipolar and mixed AFD/antipolar states. The softest island features the purely rotational states but also FE and mixed AFD/antipolar order. Unlike previous arrangements, there is a significant peak in the most unstable island at  $\approx 140i \text{ cm}^{-1}$  as a result of a significant amount of mixed AFD/antipolar modes. This suggests that such a mode character could play a role in a low-energy structure of this arrangement.

### 5. PZT V and VI

The last of the arrangements we consider together are PZT V and VI. A striking dissimilarity between these two arrangements and the rest is the increased number of unique bands in the soft space. The vast majority of these states are singly degenerate in response to the large number of uniquely coordinated ions. At the  $\Gamma$  point, both arrangements are dominated by a highly imaginary FE distortion of symmetry  $\Gamma_5^-$ . Both distortions display greater local polarization in the direction of compositional homogeneity in Ti. Local PZO units are polarized but, as in the end member PZO, Zr plays less of a role. Both arrangements feature other polar modes where, like PZT IV, Pb cation motion is in a direction perpendicular to the polarization, suggesting a dual FE and antipolar character.

Like PZT III and IV, PZT V favors isolated rotations separated by static octahedra. One example of this is  $\Gamma_3^+$  mode, where rotating layers feature a higher number of Zr sites and static layers have a higher number of Ti sites. It is true once more that purely Glazer-type rotations are not seen in the spectra of PZT V. These are replaced with Glazer-like

modes where one layer rotates more strongly than the other. The most unstable example of this is the  $\Gamma_5^+$  mode, which is strongly  $a^0a^0c^-$ -like, but the rotating layer with the higher Ti/Zr ratio rotates at a diminished amplitude. For both V and VI, the most imaginary polar branch is almost dispersionless along the path to X, resulting in the softest mode at the  $X_3^-$  and  $X_2^+$  for each arrangement, respectively. Both modes are antipolar, featuring no Pb cation motion but heavy Ti-O counter motions. Like previous PZT arrangements at this wave vector, we see non-Glazer-like isolated AFD modes and a variety of harder antipolar modes.

For PZT VI, we see that the most imaginary TO branch is not only dispersionless along the previously mentioned path but is for much of the BZ, until we see a rapid hardening as we approach  $\Lambda$ . Even here, however, the branch remains unstable. This shares some similarity with the dynamical behavior seen in the dispersion relations of  $\text{BaTiO}_3$  (BTO), but for BTO the result is a confinement of the instability to three quasi-two-dimensional slabs of  $\mathbf{q}$  space intersecting at  $\Gamma$  since the branch becomes real toward the R point. With the exception of this branch, the character of modes at the wave vectors  $(1/2, 1/2, 0)$  and  $(1/2, 1/2, 1/2)$  are rather similar. Both give rise to a large number of unique AFD/antipolar distortions similar to those described before. Notable also is the anisotropic behavior of polar branches approaching the  $\Gamma$  point from different considered directions. While most imaginary TO branches are unaffected, discontinuity can be seen clearly when comparing the  $[110]$  and  $[111]$  directions for both PZT V and VI, which is tabulated in Table IV. The fairly even distribution of states across the soft space results in a single island in the PDOS for both PZT V and VI, although, like other PZT arrangements, there is a higher density of antipolar states in the harder part of the soft space. Remarkably, despite the near-dispersionless character of the most imaginary polar branch in PZT VI, the resulting peak in the PDOS is small as a result of its isolation from other bands in the spectra and its single-fold degeneracy.

### IV. SUMMARY

We have explored the soft-mode lattice dynamics of PTO, PZO, and  $\text{PbZr}_{0.5}\text{Ti}_{0.5}\text{O}_3$  and determined the character of the most unstable modes of each arrangement. This has revealed a complex landscape of local minima and possible phase transition paths for each arrangement. It is important to emphasize that this work indicates that altering B-site ordering in a fixed concentration of Ti/Zr in PZT can in some special cases lead to the dominance of different order parameters. We find that, in general (with the exception of PZT IV), higher symmetry models like PZT I and the VCA are dominated by rotational instabilities of the  $\text{BO}_6$  octahedra which, like pure PZO, are able to couple with Pb antipolar modes at the  $\Sigma$  point, suggesting the stability of an AFE structure. Lower symmetry supercells are found to be more PTO-like, implicated by the soft zone center modes with a FE character. We suggest that this effect is the result of the presence of crystalline directions where continuous Ti-O-Ti chains exist or at least a direction where the Ti to Zr ratio is high. If this is not true (as is the case for PZT I), the more inert Zr sites act to dampen the FE distortion, allowing for rotational

instabilities to dominate. In the context of a realistic ordering of  $\text{PbZr}_{0.5}\text{Ti}_{0.5}\text{O}_3$ , these findings imply that for any given sample unless the Ti/Zr ordering is high symmetry (which is very unlikely) the dominant order parameters are likely to be zone center and FE in character. This finding agrees with the experimental observation that PZT is ferroelectric at this concentration [8]. Given the number of unique distortions in any one of the supercell models, however, it is unlikely that the ground state of these structures can be described *only* by a FE distortion. Further work could include identification of the phase transition paths, resulting in a mixed-mode ground state.

We find also that there is considerable competition with the routinely considered polar and Glazer-like rotational modes from longer wavelength antipolar modes and with non-Glazer-like AFD modes. In some cases, non-Glazer-like isolated out-of-phase rotation of  $\text{ZrO}_6$  octahedra is more unstable than Glazer  $a^0a^0c^+$  and is either closely competitive with or more unstable than  $a^0a^0c^-$  distortions. For PZT IV and V, we find *no* soft modes which result in Glazer-type rotations. We find that some soft modes can give rise to distortions characteristic of more than one order parameter. It is found that in PZT IV–VI FE order can appear simultaneously with antipolar Pb displacements. All PZT arrangements have long-wavelength soft modes displaying a dual antipolar/AFD character. It is possible that such distortions are competitive in PZT IV, suggesting a complex local minima rivaling the softer FE

distortion. Given the long wavelengths associated with these modes, there are a large number of participating atoms. It can then become costly to study their behavior with conventional plane-wave-based DFT due to well-known scaling issues. Accurate first-principles simulations of these systems will then require large-scale electronic structure methods [64].

The applicability of the VCA as a substitute for the supercell method has been investigated. While the dispersion looks strikingly similar to that of PZT I, we find that the species-specific character is considerably different. The alchemical Ti/Zr atom does not play a role in the lattice dynamics but rather is a site inert to displacement. Crucially, the softest Glazer-type rotational modes have a different classification in the VCA, becoming  $a^-b^-c^-$  and  $a^+b^+c^+$  as opposed to  $a^0a^0c^-$  and  $a^0a^0c^+$  like found in other PZT supercells and end members PTO and PZO. This quantitatively displays the inability of the VCA to represent local structural distortions.

### ACKNOWLEDGMENTS

We are grateful for computational support from the UK Materials and Molecular Modelling Hub, which is partially funded by EPSRC (EP/P020194), for which access was obtained via the UKCP consortium and funded by EPSRC Grant Ref. No. EP/P022561/1. This work also used the ARCHER UK National Supercomputing Service funded by the UKCP consortium EPSRC Grant Ref. No. EP/P022561/1.

- 
- [1] B. Jaffe, *Piezoelectric Ceramics* (Elsevier, New York, 2012), Vol. 3.
- [2] C. Oliveira, E. Longo, J. Varela, and M. Zaghete, *Ceram. Int.* **40**, 1717 (2014).
- [3] N. Izyumskaya, Y.-I. Alivov, S.-J. Cho, H. Morkoç, H. Lee, and Y.-S. Kang, *Crit. Rev. Solid State Mater. Sci.* **32**, 111 (2007).
- [4] T. Gururaja, W. A. Schulze, L. E. Cross, R. E. Newnham, B. A. Auld, and Y. J. Wang, *IEEE Trans. Sonics Ultrason.* **32**, 481 (1985).
- [5] Z. Chi and Q. Xu, *Int. J. Adv. Robotic Syst.* **11**, 182 (2014).
- [6] A. M. Kadin and S. B. Kaplan, *IEEE Trans. Appl. Supercond.* **27**, 1801105 (2017).
- [7] S. C. Pais, Piezoelectricity-induced room temperature superconductor (2019).
- [8] Y. M. Jin, Y. U. Wang, A. G. Khachatryan, J. F. Li, and D. Viehland, *Phys. Rev. Lett.* **91**, 197601 (2003).
- [9] J. C. Agar, R. V. K. Mangalam, A. R. Damodaran, G. Velarde, J. Karthik, M. B. Okatan, Z. H. Chen, S. Jesse, N. Balke, S. V. Kalinin, and L. W. Martin, *Adv. Mater. Interfaces* **1**, 1400098 (2014).
- [10] B. Noheda, D. E. Cox, G. Shirane, J. A. Gonzalo, L. E. Cross, and S.-E. Park, *Appl. Phys. Lett.* **74**, 2059 (1999).
- [11] G. Catalan, A. Lubk, A. H. G. Vlooswijk, E. Snoeck, C. Magen, A. Janssens, G. Rispens, G. Rijnders, D. H. A. Blank, and B. Noheda, *Nat. Mater.* **10**, 963 (2011).
- [12] R. Nelmes and W. Kuhs, *Solid State Commun.* **54**, 721 (1985).
- [13] Z. G. Fthenakis and I. Ponomareva, *Phys. Rev. B* **96**, 184110 (2017).
- [14] K. M. Rabe, Antiferroelectricity in oxides: a reexamination, in *Functional Metal Oxides: New Science and Novel Applications*, edited by S. B. Ogale, T. V. Venkatesan, and M. Blamire (Wiley-VCH, Weinheim, 2013), Chap. 7, pp. 221–244.
- [15] A. K. Tagantsev, K. Vaideeswaran, S. B. Vakhrushev, A. V. Filimonov, R. G. Burkovsky, A. Shaganov, D. Andronikova, A. I. Rudskoy, A. Q. R. Baron, H. Uchiyama, D. Chernyshov, A. Bosak, Z. Ujma, K. Roleder, A. Majchrowski, J.-H. Ko, and N. Setter, *Nat. Commun.* **4**, 2229 (2013).
- [16] J. Hlinka, T. Ostapchuk, E. Buixaderas, C. Kadlec, P. Kuzel, I. Gregora, J. Kroupa, M. Savinov, A. Klic, J. Drahokoupil, I. Etxebarria, and J. Dec, *Phys. Rev. Lett.* **112**, 197601 (2014).
- [17] B. K. Mani, S. Lisenkov, and I. Ponomareva, *Phys. Rev. B* **91**, 134112 (2015).
- [18] C. V. Raman and T. M. K. Nedungadi, *Nature (London)* **145**, 147 (1940).
- [19] W. Cochran, *Phys. Rev. Lett.* **3**, 412 (1959).
- [20] W. Cochran, *Adv. Phys.* **9**, 387 (1960).
- [21] P. W. Anderson, Physics of Dielectrics, *Izv. Akad. Nauk SSSR*, 290 (1960).
- [22] N. Siconolfi, B. Ravel, Y. Yacoby, E. A. Stern, F. Dogan, and J. J. Rehr, *Phys. Rev. B* **50**, 13168 (1994).
- [23] P. Marton and C. Elsässer, *Phys. Status Solidi B* **248**, 2222 (2011).
- [24] J. L. Blok, D. H. A. Blank, G. Rijnders, K. M. Rabe, and D. Vanderbilt, *Phys. Rev. B* **84**, 205413 (2011).
- [25] Z. Wu and H. Krakauer, *Phys. Rev. B* **68**, 014112 (2003).
- [26] S. Kim, W.-J. Lee, Y.-H. Cho, M. Shim, and S. Kim, *Jpn. J. Appl. Phys.* **52**, 091101 (2013).

- [27] I. Grinberg, V. Cooper, and A. Rappe, *Phys. Rev. B* **69**, 144118 (2004).
- [28] C. Bungaro and K. M. Rabe, *Phys. Rev. B* **65**, 224106 (2002).
- [29] L. Bellaïche and D. Vanderbilt, *Phys. Rev. B* **61**, 7877 (2000).
- [30] N. J. Ramer and A. M. Rappe, *Phys. Rev. B* **62**, R743 (2000).
- [31] S.-Y. Liu, Q.-S. Shao, D.-S. Yu, Y.-K. Lü, D.-J. Li, Y. Li, and M.-S. Cao, *Chin. Phys. B* **22**, 017702 (2013).
- [32] A. J. Bell, *J. Mater. Sci.* **41**, 13 (2006).
- [33] A. Bogdanov, A. Mysovsky, C. J. Pickard, and A. V. Kimmell, *Phys. Chem. Chem. Phys.* **18**, 28316 (2016).
- [34] A. M. Glazer, *Acta Crystallogr., Sect. B* **28**, 3384 (1972).
- [35] A. M. Glazer, *Acta Crystallogr. Sect. A* **31**, 756 (1975).
- [36] X. Gonze, F. Jollet, F. A. Araujo, D. Adams, B. Amadon, T. Applencourt, C. Audouze, J.-M. Beuken, J. Bieder, A. Bokhanchuk *et al.*, *Comput. Phys. Commun.* **205**, 106 (2016).
- [37] X. Gonze, B. Amadon, P.-M. Anglade, J.-M. Beuken, F. Bottin, P. Boulanger, F. Bruneval, D. Caliste, R. Caracas, M. Côté *et al.*, *Comput. Phys. Commun.* **180**, 2582 (2009).
- [38] D. R. Hamann, *Phys. Rev. B* **88**, 085117 (2013).
- [39] M. van Setten, M. Giantomassi, E. Bousquet, M. Verstraete, D. Hamann, X. Gonze, and G.-M. Rignanese, *Comput. Phys. Commun.* **226**, 39 (2018).
- [40] H. J. Monkhorst and J. D. Pack, *Phys. Rev. B* **13**, 5188 (1976).
- [41] J. P. Perdew, A. Ruzsinszky, G. I. Csonka, O. A. Vydrov, G. E. Scuseria, L. A. Constantin, X. Zhou, and K. Burke, *Phys. Rev. Lett.* **100**, 136406 (2008).
- [42] M. A. Marques, M. J. Oliveira, and T. Burnus, *Comput. Phys. Commun.* **183**, 2272 (2012).
- [43] Y. Zhang, J. Sun, J. P. Perdew, and X. Wu, *Phys. Rev. B* **96**, 035143 (2017).
- [44] S. A. Mabud and A. M. Glazer, *J. Appl. Crystallogr.* **12**, 49 (1979).
- [45] E. Sawaguchi, *J. Phys. Soc. Jpn.* **8**, 615 (1953).
- [46] X. Gonze and C. Lee, *Phys. Rev. B* **55**, 10355 (1997).
- [47] S. Baroni, S. de Gironcoli, A. D. Corso, and P. Giannozzi, *Rev. Mod. Phys.* **73**, 515 (2001).
- [48] W. Zhong, R. D. King-Smith, and D. Vanderbilt, *Phys. Rev. Lett.* **72**, 3618 (1994).
- [49] C. H. Henry and J. J. Hopfield, *Phys. Rev. Lett.* **15**, 964 (1965).
- [50] X. Gonze, *Phys. Rev. B* **55**, 10337 (1997).
- [51] P. Ghosez, in *Fundamental Physics of Ferroelectrics 2000: Aspen Center for Physics Winter Workshop*, edited by R. E. Cohen and R. A. Mewaldt, AIP Conf. Proc. No.535 (AIP, New York, 2000), pp. 102–110.
- [52] A. Togo and I. Tanaka, *Scr. Mater.* **108**, 1 (2015).
- [53] See Supplemental Material at <http://link.aps.org/supplemental/10.1103/PhysRevB.100.224305> for a full tabulation of the soft modes for each calculation, a demonstration of the equivalence of DFPT to the FDM, and the full phonon dispersion curves (including real branches) for each calculation.
- [54] L. Vegard, *Z. Phys.* **5**, 17 (1921).
- [55] P. E. Blöchl, O. Jepsen, and O. K. Andersen, *Phys. Rev. B* **49**, 16223 (1994).
- [56] H. T. Stokes and D. M. Hatch, *J. Appl. Crystallogr.* **38**, 237 (2005).
- [57] B. J. Campbell, H. T. Stokes, D. E. Tanner, and D. M. Hatch, *J. Appl. Crystallogr.* **39**, 607 (2006).
- [58] H. Miranda, Visualization of phonons, 2019, <https://henriquemiranda.github.io/phononwebsite/phonon.html>.
- [59] M. I. Aroyo, J. M. Perez-Mato, C. Capillas, E. Kroumova, S. Ivantchev, G. Madariaga, A. Kirov, and H. Wondratschek, *Z. Kristallogr.-Cryst. Mater.* **221**, 15 (2006).
- [60] P. Ghosez, E. Cockayne, U. V. Waghmare, and K. M. Rabe, *Phys. Rev. B* **60**, 836 (1999).
- [61] J. Íñiguez, M. Stengel, S. Prosandeev, and L. Bellaïche, *Phys. Rev. B* **90**, 220103(R) (2014).
- [62] M. I. Aroyo, D. Orobengoa, G. de la Flor, E. S. Tasci, J. M. Perez-Mato, and H. Wondratschek, *Acta Crystallogr., Sect. A: Found. Adv.* **70**, 126 (2014).
- [63] G. Shirane, J. D. Axe, J. Harada, and J. P. Remeika, *Phys. Rev. B* **2**, 155 (1970).
- [64] D. R. Bowler and T. Miyazaki, *Rep. Prog. Phys.* **75**, 036503 (2012).